Journal of Power Sources 191 (2009) 510–519

Contents lists available at ScienceDirect

Journal of Power Sources

journal homepage: www.elsevier.com/locate/jpowsour

# New theoretical model for convergent nozzle ejector in the proton exchange membrane fuel cell system

Yinhai Zhu*, Yanzhong Li

*School of Energy and Power Engineering, Xi'an Jiaotong University, Xi'an 710049, PR China*

ARTICLE INFO

*Article history:*
Received 15 December 2008
Accepted 5 February 2009
Available online 20 February 2009

*Keywords:*
Ejector
Model
Performance
PEM fuel cell
Anode recirculation

ABSTRACT

A new theoretical model for the convergent nozzle ejector in the anode recirculation line of the polymer electrolyte membrane (PEM) fuel cell system is established in this paper. A velocity function for analyzing the flow characteristics of the PEM ejector is proposed by employing a two-dimensional (2D) concave exponential curve. This treatment of velocity is an improvement compared to the conventional 1D "constant area mixing" or "constant pressure mixing" ejector theories. The computational fluid dynamics (CFD) technique together with the data regression and parameter identification methods are applied in the determination of the velocity function's exponent. Based on the model, the anode recirculation performances of a hybrid PEM system are studied under various stack currents. Results show that the model is capable of evaluating the performance of ejector in both the critical mode and subcritical mode.



## 1. Introduction

The polymer electrolyte membrane (PEM) fuel cell is considered the best candidate to replace the combustion power generator because of its capability of high power density, low operating temperature, and short start-up time. The fuel, hydrogen, is usually stored in a highly pressurized tank in order to increase its volume density, while the pressure of the fuel cell stack is relatively low. The high-pressure difference between hydrogen tank and fuel cell stack, which contains abundant pressure potential energy, can be utilized by means of an ejector. With no moving parts and less maintenance, the ejector uses the high-pressure hydrogen as the primary fluid to suck the anodic exhaust (secondary flow). Unconsumed hydrogen in the anodic exhaust is recycled to the fuel cell stack so that the fuel utilization efficiency is increased [1–3].

Unlike ejectors applied in refrigeration and SOFC anode recirculation systems, the ejector in the anode recirculation line of PEM fuel cell system usually has a convergent not convergent–divergent nozzle to convert the primary flow's pressure energy to kinetic energy. The usage of the convergent nozzle ejector is to decrease the condensation of water vapor in the ejector due to the low temperature of the primary and secondary flows in the PEM fuel cell system. A clear understanding of the working principle and performance characteristic of a convergent nozzle ejector is required for the performance evaluation and analysis of the anode recirculation PEM fuel cell system.

The ejectors are widely used in industry and have been studied for decades using theoretical, empirical or numerical methods [4–6]. However, most of the existing ejector models are developed based on one-dimensional (1D) technique for cooling and refrigeration [7–9] and SOFC [10–13] applications. There are very few researches for the ejector applied in the fuel recirculation line of the PEM fuel cell system.

Karnik et al. studied an ejector based PEM fuel cell anode recirculation system. The ejector was modeled based on the 1D simplification and the "constant area mixing" assumption [14,15]. Bao et al. proposed models for a PEM fuel cell system with an ejector based recirculation line, however only the ejector performances in the critical operational condition were analyzed [16]. He et al. investigated a hybrid fuel delivery system in the PEM fuel cell consisting of two supply and two recirculation lines. The ejector was assumed work in the critical mode and the primary and secondary flows were analyzed based on the 1D "constant pressure mixing" theory [17]. According to the ejector flow theory, the ejector performance is divided into three operational modes, i.e., back flow, subcritical and critical modes by the operating conditions [4,8]. The ejector may work in the subcritical mode or even back flow mode during start up, load changes and shut down. In these cases, the flow characteristic becomes complicated and unexpected fluctuations in the anode recirculation line could occur.

In this paper, we aim to develop a simple and accurate theoretical model for both critical and subcritical operating ejector in the hybrid PEM fuel cell system. The paper is organized as follows:

* Corresponding author. Tel.: +86 29 82668738; fax: +86 29 82668725.
*E-mail addresses:* yinhai.zhu@gmail.com (Y. Zhu), yzli-epe@mail.xjtu.edu.cn (Y. Li).

0378-7753/$ – see front matter © 2009 Elsevier B.V. All rights reserved.
doi:10.1016/j.jpowsour.2009.02.014

**Nomenclature**

| | |
|---|---|
| $A$ | area ($m^2$) |
| $C_p$ | specific heat of gas at constant pressure ($J\,kg^{-1}\,K^{-1}$) |
| $D$ | diameter (m) |
| $m$ | mass (kg) |
| $M$ | Mach number |
| $Mo$ | molecular weight ($kg\,mol^{-1}$) |
| $n$ | molar flow rate ($mol\,s^{-1}$) |
| $n_v$ | exponent of the 2D curve |
| $P$ | pressure (Pa) |
| $r$, $R$ | radius (m) |
| $R_g$ | gas constant ($J\,kg^{-1}\,K^{-1}$) |
| $R_u$ | universal gas constant ($J\,mol^{-1}\,K^{-1}$) |
| $T$ | temperature (K) |
| $v$, $V$ | velocity ($m\,s^{-1}$) |
| $W$ | mass flow rate ($kg\,s^{-1}$) |
| $y$ | mass fraction |

*Greek symbols*

| | |
|---|---|
| $\beta_P$ | pressure ratio, $P_S^{0.8}/P_P^{1.1}$ (pressure in bar) |
| $\beta_D$ | diameter ratio, $D_m/D_t$ |
| $\kappa$ | specific heat ratio of gas |
| $\omega$ | recirculation ratio, $W_S/W_P$ |
| $\rho$ | density ($kg\,m^{-3}$) |
| $\Psi_P$ | isentropic coefficient of primary flow |
| $\Psi_S$ | isentropic coefficient of secondary flow |
| $\xi_{exp}$ | coefficient accounting for friction loss during the mixing process |

*Subscripts*

| | |
|---|---|
| an | anode flow channel |
| MEA | membrane |
| P | primary flow (i.e. inlet fuel) |
| S | secondary flow (i.e. anode recycling gas) |
| B | ejector exit |
| t | nozzle throat |
| 0 | ejector inlet |
| 1 | nozzle exit |
| 2 | mixing chamber inlet |
| 3 | ejector exit |
| in | inlet |
| out | outlet |

*Superscript*

| | |
|---|---|
| $i$ | chemical component |

1. The working principle of an ejector based anode recirculation PEM fuel cell system is described and the PEM fuel cell model is briefly introduced in Section 2.
2. In Section 3, a new theoretical model for the convergent nozzle ejector is constructed by employing a 2D exponential function to compute fluid velocity near the ejector inner walls. Governing equations for computing the mass flow rate, recirculation ratio and the ejector exit temperature are derived based on the thermodynamic and fluid dynamic principles.
3. A method for determination of the 2D exponential function is proposed in Section 4. A set of ejector geometries and working conditions are first simulated using the computational fluid dynamics (CFD) technique. Then the simulation results are treated using the data regression and parameter identification methods to find out the relation between the exponent and the geometries and working conditions.
4. In Section 5, the detailed application procedure for the ejector model is presented. Comparisons are made between the model results and the corresponding CFD data.
5. In Section 6, a hybrid PEM fuel cell system integrated with an ejector at the anode recirculation line is studied using the proposed model. Behaviors of the anode recirculation line are obtained and analyzed.

## 2. PEM fuel cell system

### 2.1. Working principle of anode recirculation PEM fuel cell system

A PEM fuel cell system with an ejector in the anode recirculation line is shown in Fig. 1. It mainly consists of three components: a PEM fuel cell stack, an ejector and a humidifier. The structure of a PEM fuel cell can be described as two electrodes (anode and cathode) separated by a membrane. High-pressure hydrogen entering the ejector is called the primary flow. Inside the ejector, the primary flow expands in a convergent nozzle in which its pressure potential energy converts into kinetic energy, resulting in a low-pressure region. The anode recycle gas (secondary flow) is entrained into the ejector. The two flows mix in the ejector then discharge to the humidifier. According to Refs. [14–17], the functions of ejector in the anode recirculation line are

- Utilize the pressure potential energy of hydrogen otherwise wasted;
- Recycle the unconsumed hydrogen to the fuel cell to increase the fuel usage efficiency;
- Regulate the anode humidity with the recycle gas;
- Raise the secondary flow pressure to meet the fuel cell pressure at the required level.

The ejector performance is usually evaluated by the recirculation ratio $\omega$, which is defined as

$$\omega = W_S/W_P \tag{1}$$

where $W_P$ and $W_S$ are the mass flow rates of the primary and secondary flows, respectively.

In the humidifier, the gas humidification is considered to be perfect. For a volume of hydrogen gas with water vapor and liquid water, the water activity $a_w$ and relative humidity $\Phi$ are defined as

$$a_w = \frac{m_{H_2O}}{m_{v,sat}}; \qquad \phi = \frac{P_v}{P_{v,sat}} \tag{2}$$

where $m_{H_2O}$, $m_{v,sat}$ is the total water and saturation mass of water vapor in the volume, respectively. $P_v$ is the partial pressure of water vapor in the mixture. $P_{v,sat}$ is the saturation pressure of the water vapor, which is related to the mixture temperature [18].

In the anode, Hydrogen dissociates into protons that flow through the membrane to the cathode. At the same time, electrons lost from hydrogen which are collected as electrical current by an external circuit linking the two electrodes. Air flows to the cathode where oxygen combines with the electrons. The chemical reactions taking place at the two electrodes are listed as follows:

$$\text{Anodereaction}: \quad 2H_2 \rightarrow 4H^+ + 4e \tag{3}$$

$$\text{Cathodereaction}: \quad O_2 + 4H^+ + 4e \rightarrow 2H_2O \tag{4}$$

$$\text{Overallreaction}: \quad O_2 + 2H_2 \rightarrow 2H_2O + \text{heat} \tag{5}$$

### 2.2. PEM fuel cell model

The model for the PEM fuel cell consists of two parts: one is about thermodynamic equations to calculate the temperature and

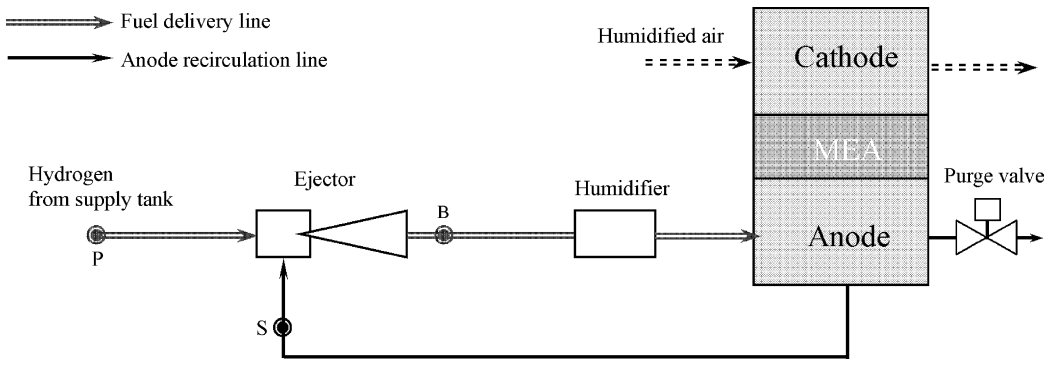


**Fig. 1.** Ejector based anode recirculation PEM fuel cell system.

mass flow rate, and the other is electrochemical part that computes the cell potential and power. As the main purpose of this work is to study the performance of fuel delivery and anode recirculation lines, only the performance of anode side is analyzed. The steady-state PEM fuel cell model adopted in this work is briefly introduced as follows:

The mass conservation equations of the anode are

$$W_{H_2,an,in} = W_{H_2,an,out} + W_{H_2,reacted} \quad (6)$$

$$W_{v,an,in} = W_{v,an,out} - W_{v,MEA} \quad (7)$$

where $W_{H_2,an,in}$ and $W_{v,an,in}$ are the mass flow rates of hydrogen and water vapor entering the anode flow channel, which are related to the ejector and humidifier's operational conditions:

$$W_{H_2,an,in} = W_P + y_{H_2,an,out} W_S \quad (8)$$

$$W_{v,an,in} = \frac{y_{v,hum}}{1 - y_{v,hum}} W_{H_2,an,in} \quad (9)$$

where $W_P$ and $W_S$ in Eq. (8) are derived from the ejector model presented in Sections 3–5. $y_{v,hum}$ is the mass fraction of the water vapor in the humidifier.

In Eq. (6), $W_{H_2,reacted}$, which means the mass rate of hydrogen consumed in the anode, is described as [19]:

$$W_{H_2,reacted} = N_{cell} \frac{IMo_{H_2}}{2F} \quad (10)$$

$W_{v,MEA}$ in Eq. (7) is the transport rate of water vapor through the membrane from the anode to the cathode resulting from diffusion, electro-osmotic drag force, and pressure gradient:

$$W_{v,MEA} = \alpha_{net} N_{cell} \frac{IMo_{H_2O}}{F} \quad (11)$$

where $\alpha_{net}$ is the net water transfer coefficient which is defined as the ratio of the net water flux in PEM to the ion flux [19,20].

The expression of the voltage of a single cell is

$$V_{cell} = E + \eta_{act} + \eta_{ohmic} + \eta_{diff} \quad (12)$$

where the thermodynamic potential of the $H_2 + O_2$ reaction, $E$, can be further expressed by [21]:

$$E = 1.229 - 0.85 \times 10^{-3}(T - 298.15) + 4.3085 \times 10^{-5} T \ln[p^*_{H_2}(p^*_{O_2})^{0.5}] \quad (13)$$

The parametric expression of the activation over potential $\eta_{act}$, ohmic over potential $\eta_{ohmic}$ and diffusion over potential $\eta_{diff}$ can be written as follows:

$$\eta_{act} = \xi_1 + \xi_2 T_{cell} + \xi_3 T_{cell} \ln(C^*_{O2}) + \xi_4 T_{cell} \ln(I) \quad (14)$$

$$\eta_{ohmic} = -I \cdot R^{internal} \quad (15)$$

$$\eta_{diff} = m \exp(nI) \quad (16)$$

where the parameters $\xi 1$–$\xi 4$, $m$ and $n$ can be found in literatures [21–24].

The thermodynamic efficiency of the PEM fuel cell can be evaluated by [25]:

$$Eff = \frac{2n_{cell} V_{cell} I}{W_{H_2,reacted} \cdot LHV_{H_2}} \quad (17)$$

## 3. Ejector theoretical model development

A convergent nozzle ejector applied in the anode recirculation line of PEM fuel cell is schematically shown in Fig. 2(a). The ejector has a convergent nozzle not convergent–divergent nozzle as the flow expansion device. According to the characteristic of the secondary flow, the ejector performance are divided into three operational modes: back flow, subcritical and critical as depicted in Fig. 2(b) [4,8]. The secondary mass flow rate, which is very sensitive to the operational conditions in the subcritical mode and keeps near constant in the critical mode.

Without loss of generality, the following assumptions are made in developing a model for the convergent nozzle ejector used in the PEM fuel cell system:

1. The primary flow is treated as the ideal gas.
2. The primary flow velocity is uniform in the radial direction inside the ejector.
3. The velocity of the secondary flow inside the ejector is non-uniformly distributed in the radial direction and there exists velocity boundary layer near ejector inner walls.
4. Pressure and temperature of both the primary and the secondary flows are uniformly distributed in the radial direction of ejector.
5. The isentropic relations hold in calculating friction losses.

### 3.1. Primary flow

According the flow characteristic of the convergent nozzle, the flow through the convergent nozzle is divided into two different regions: subsonic and sonic flow by the pressure ratio $P_S/P_P$. The relation between the pressure ratio and the mass flow rate is shown in Fig. 3. Due to without a divergent part, the flow cannot reach sonic flow condition when the pressure ratio is greater than the critical value $\upsilon_{cr}$. The critical pressure ratio $\upsilon_{cr}$ of a convergent nozzle can be written as

$$\nu_{cr} = \left(\frac{2}{\kappa + 1}\right)^{\kappa/(\kappa-1)} \quad (18)$$

For sonic flow (when $P_{P,0} \geq P_{S,0}/\upsilon_{cr}$), the primary flow rate $m_P$ can be obtained by using the isentropic flow relations and energy

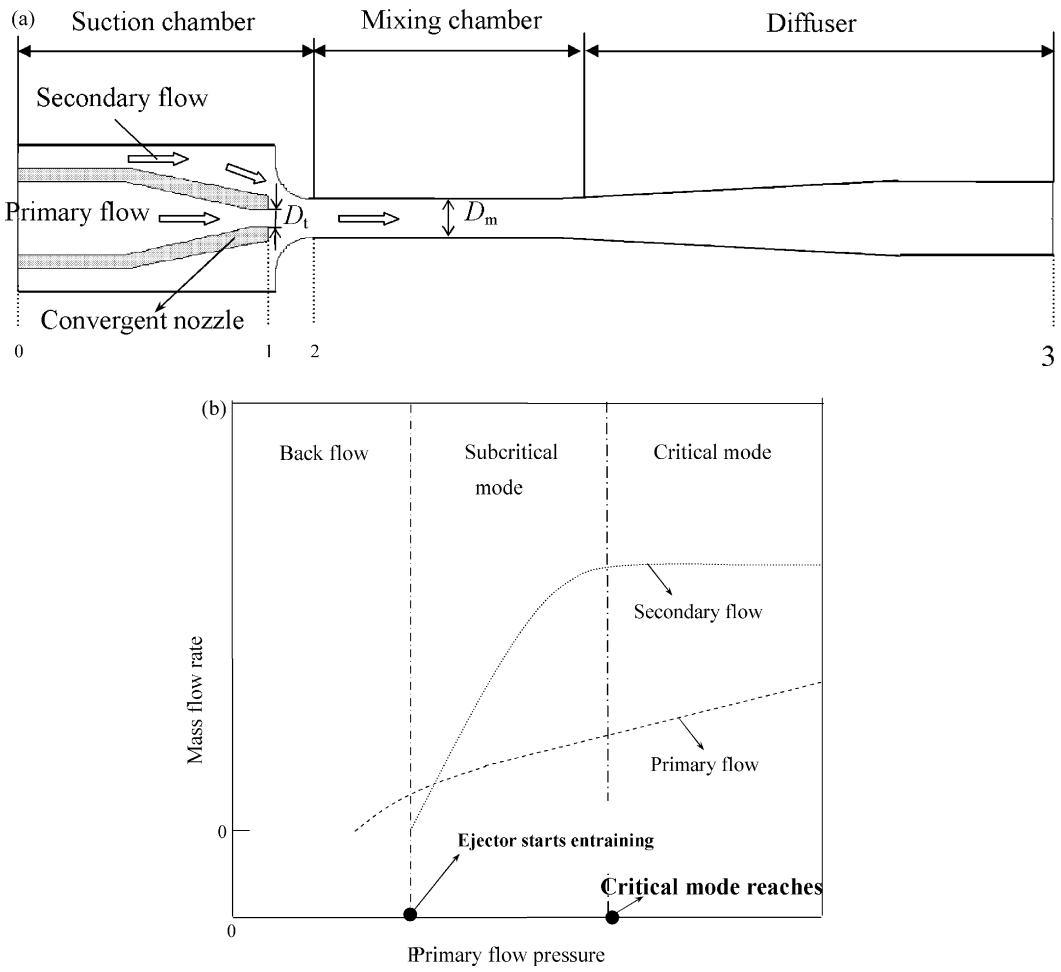


**Fig. 2.** Schematic diagram showing geometries and operational modes of an ejector (a) Ejector geometries; (b) Operational modes.

balance law:

$$W_P = P_P A_t \sqrt{\frac{\psi_P k}{R_g T_P}} \left(\frac{2}{\kappa+1}\right)^{(\kappa+1)/(2(\kappa-1))} \tag{19}$$

and the Mach number at the nozzle throat is 1, i.e.:

$$M_t = 1 \tag{20}$$

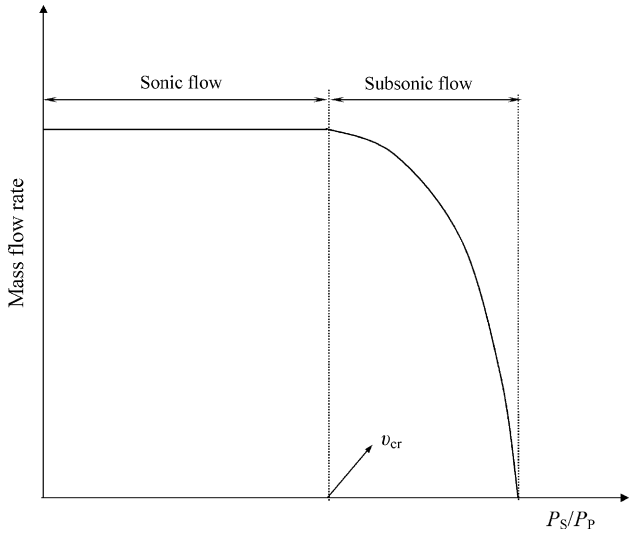


**Fig. 3.** Influence of pressure ratio on mass flow rate of a convergent nozzle.

For subsonic flow (when $P_P < P_S/\upsilon_{cr}$), the primary flow rate $m_P$ and the Mach number at the nozzle throat $M_t$ are calculated from:

$$W_P = P_P A_t \sqrt{\frac{2\psi_P \kappa[(P_S/P_P)^{2/\kappa} - (P_S/P_P)^{(1+\kappa)/\kappa}]}{(\kappa-1)R_g T_P}} \tag{21}$$

$$M_t = \sqrt{\frac{2[1-(P_S/P_P)^{(\kappa-1)/\kappa}]}{(\kappa-1)}} \tag{22}$$

where $\Psi_P$ is the isentropic coefficient taking into account the flow friction loss.

The primary flow expands fully in the suction chamber. The ambient pressure of the expansion flow can be represented by the secondary flow pressure $P_S$. Using the isentropic flow and energy balance laws for the primary flow from Section 1 to Section 2, we have:

$$\frac{P_P}{P_S} = \left[1 + \frac{1}{2}(\kappa-1)M_{P,2}^2\right]^{\kappa/(\kappa-1)} \tag{23}$$

$$\frac{T_P}{T_{P,2}} = 1 + \frac{1}{2}(\kappa-1)M_{P,2}^2 \tag{24}$$

$$V_{P,2} = M_{P,2}\sqrt{\kappa R_g T_{P,2}} \tag{25}$$

$$\frac{\xi_{exp} D_{P,2}}{D_t} = \left[\frac{2+(\kappa-1)M_{P,2}^2}{2+(\kappa-1)M_t^2}\right]^{(\kappa+1)/(4(\kappa-1))} \left(\frac{M_t}{M_{P,2}}\right)^{0.5} \tag{26}$$

where $\xi_{exp}$ is a coefficient accounting for the frictional loss due to the mixing process of the two flows.

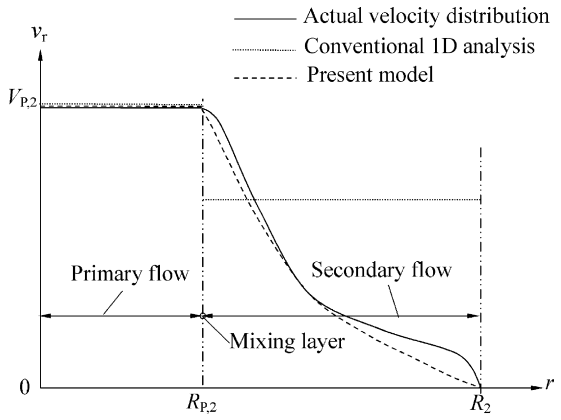


**Fig. 4.** Velocity distribution in Section 2 of a convergent nozzle ejector.

### 3.2. Secondary flow

The ejector performance is significantly affected by the flow characteristics in Section 2 [9]. In Section 2, a mixing layer separates the primary flow and the secondary flow. The secondary flow outside the layer has a non-linear velocity distribution due to the turbulent flow and fluid viscosity as shown in Fig. 4. In the conventional 1D analysis, both velocities of the primary flow and secondary flow are treated uniform in the radial direction. Obviously, this method will induce uncertainty in the ejector modeling.

It is important to note that the velocity distribution in the convergent nozzle ejector is different from that in a convergent–divergent nozzle ejector. The velocity of the primary flow at nozzle exit is relatively low in the convergent nozzle ejector due to no divergent part. Therefore, the primary flow in the convergent nozzle ejector cannot accelerate the secondary flow effectively like the convergent–divergent nozzle ejector do, leading to a concave velocity distribution of the secondary flow as depicted in Fig. 4.

In order to describe the concave velocity distribution curve, we propose the following governing equations for the velocities of primary flow and secondary flow in Section 2

$$v_r = \begin{cases} V_{P,2} & (0 \le r \le R_{P,2}) \\ V_{P,2}\left(\dfrac{R_2 - r}{R_2 - R_{P,2}}\right)^{n_v} & (R_{P,2} < r \le R_2) \end{cases} \tag{27}$$

where $n_v$ is the exponent of the velocity function. $n_v$ is supposed to be greater than 1 ($n_v > 1$) for a convergent nozzle ejector. The graph of $v_r$ versus $r$ is given as the dashed curve in Fig. 4. Clearly, it is closer to the actual velocity distribution than the 1D approach.

Based on this 2D velocity function, we define the mean mass flow rate of secondary flow at Section 2 as

$$W_S = \int_{R_{P,2}}^{R_2} \bar{\rho} v_r dA \tag{28}$$

where $\bar{\rho}$ stands for the average density of secondary flow. Substituting Eq. (27) into Eq. (28) leads to the following integral equation:

$$W_S = \frac{2\pi V_{P,2}\bar{\rho}_S}{(R_2 - R_{P,2})^{n_v}} \int_{R_{P,2}}^{R_2} (R_2 - r)^{n_v} r dr \tag{29}$$

By evaluating the integral of Eq. (29), the mass flow rate of the secondary flow can finally be expressed as

$$W_S = \frac{2\pi\bar{\rho}_S V_{P,2}(R_2 - R_{P,2})(R_2 + R_{P,2} + n_v R_{P,2})}{(n_v + 1)(n_v + 2)} \tag{30}$$

By using the conditions of $V_{S,2} = W_S/(\rho_S A_{S,2})$ and $A_{S,2} = \pi (R_2^2 - R_{P,2}^2)$, we obtain the average velocity of the secondary flow in Section 2

$$V_{S,2} = \frac{2V_{P,2}(R_2 + R_{P,2} + n_v R_{P,2})}{A_{S,2}(n_v + 1)(n_v + 2)(R_2 + R_{P,2})} \tag{31}$$

where the average density of the secondary flow is given as

$$\bar{\rho}_S = \frac{P_S}{R_g T_S} = \frac{P_S}{T_S} \frac{\sum_i n_S^i Mo^i}{R_u \sum_i n_S^i} \tag{32}$$

### 3.3. Energy balance of two flows

For an ideal gas, the energy balance of the primary and secondary flow in the ejector can be described by

$$\sum_i W_P^i C_p^i T_P + \sum_i W_S^i C_p^i T_S = \sum_i (W_P^i + W_S^i) C_p^i T_3 + E_{loss} \tag{33}$$

where the energy loss, $E_{loss}$, of the primary and secondary flows in the ejector can be approximated as

$$E_{loss} = \frac{1}{2}(1 - \psi_P) W_P V_{P,2}^2 + \frac{1}{2}(1 - \psi_S) W_S V_{S,2}^2 \tag{34}$$

**Remark.** The velocity of the secondary flow is accurately modeled by a 2D exponential function in the new model. Because of this improvement, the present model is capable of predicting the ejector performance within less uncertainties compared to the conventional 1D analysis. Additionally, the treatment of the secondary flow velocity makes the new model simpler than the conventional "constant area mixing" or "constant pressure mixing" theory. For example, the model for calculating $W_S$ only consists of one algebraic equation (Eq. (30)).

Note that the exponent $n_v$ in Eq. (30) is very important, which decides the pattern of the concave velocity distribution curve. The value of $n_v$ is not a constant, which will be influenced by the ejector geometries and working conditions. In order to determine the exponent $n_v$, a numerical method based on the CFD technique is proposed in Section 4.

## 4. Velocity exponent determination

In this section, the numerical CFD method is first introduced including the grid structure building, solution strategy constructing, turbulence model selecting and boundary conditions setting. The CFD method for the ejector flow simulation has been experimentally validated previously [26]. Based on this method, four different ejector geometries and 32 working conditions are simulated. Finally, the data regression and parameter identification methods are used to determine the velocity exponent $n_v$ based on the obtained simulation results.

### 4.1. Numerical CFD method

The CFD method is capable of producing details of the flow field and fluid properties based on numerical solutions of the flow domain. The flow, heat transfer, radiation, turbulence, etc. at any given operating conditions and model geometries can be simulated. Data that is difficult to obtain in an experiment can be easily analyzed using CFD.

The commercial software Gambit 2.2 and FLUENT 6.2 are used as the grid generator and the CFD solver in this numerical study, respectively. The ejector geometries are modeled in a 2D domain in the Gambit. The grids are only adapted at the locations with significant flow changes such as velocity boundary and shock position

**Table 1**
Four ejector geometries.

| Ejector number | $D_t$ (mm) | $D_m$ (mm) | $\beta_D$ |
|---|---|---|---|
| 1 | 2.1 | 5.2 | 2.48 |
| 2 | 3.2 | 7.2 | 2.25 |
| 3 | 2.8 | 8 | 2.86 |
| 4 | 2.4 | 6.4 | 2.67 |

for faster computation speed. 3D effects can be reflected by the 2D ejector model since the axi-symmetric solver is applied.

The flow inside the ejector is governed by the compressible steady-state turbulent form of the flow governing equations. The non-linear governing equations are solved using the "Segregated-implicit" solver [27]. The species transport model is used to deal with the mixture fluid flow. The second-order upwind scheme is adopted to discretize convective terms. The SIMPLEC algorithm is applied to obtain the pressure field. Moreover, the "RNG $k$–$\varepsilon$ model" is selected as the turbulence model for its ability to better predict ejector performance than other turbulence models [26].

The working fluid of the primary flow is pure hydrogen, while the secondary flow is composed of hydrogen and water vapor. The density is obtained using the ideal gas relationship. Boundary conditions of the primary flow and the secondary flow inlets are set as "pressure inlet" condition, and the "pressure outlet" condition is adopted on the ejector outlet. For each simulation, the solution is iterated until convergence is achieved (residue for each equation is less than $10^{-4}$).

### 4.2. Data regression

The pressures $P_P$ and $P_S$ and diameters $D_t$ and $D_m$ affect the velocity distribution inside the ejector, so as to decide the velocity exponent $n_v$. In order to find out the relations between the pressures, diameters and $n_v$, we first investigate the influence of $P_P$ and $P_S$ on $n_v$ at the same ejector geometries, then study the effect of $D_t$ and $D_m$ at constant working conditions.

Four ejectors geometries are created as shown in Table 1. In these ejectors, the diameter ratio $\beta_D(D_m/D_t)$ is in the range of 2.25–2.86. According to the typical operating conditions of PEM fuel cells, three pressure groups are designed: $P_B$ = 3 bar and $P_S$ = 2.8 bar; $P_B$ = 1.5 bar and $P_S$ = 1.35 bar; $P_B$ = 1.1 bar and $P_S$ = 1.0 bar. For each pressure group, the ejectors are simulated by varying the primary flow pressure $P_P$. The outputs of the CFD model simulation include the two mass flow rates $W_S$ and $W_P$ and the ejector exit temperature.

Substituting $W_S$ and $W_P$ into Eqs. (19)–(26) and Eqs. (31)–(32), the corresponding $n_v$ can be computed by an iterative calculation. As shown in Fig. 5, it is found that $n_v$ has a exponential relation with $P_S^{0.8}/P_P^{1.1}$ using the data regression analysis. Results in Fig. 6 show that $n_v$ is finely linear with $D_m/D_t$ in all the studied cases.

### 4.3. Parameter identification

Based on the data regression studies, it is reasonable to assume that $n_v$ has the following expression:

$$n_v = A_1 \ \exp(\beta_P/0.05) + A_2\beta_D + A_3 \tag{35}$$

where $\beta_P = P_S^{0.8}/P_P^{1.1}$ (here $P_S$ and $P_P$ is in bar); $\beta_D = D_m/D_t$; $A_1$, $A_2$ and $A_3$ are parameters which can be determined by the identification method introduced as follows:

If $N$ experimental or numerical CFD tests are conducted for different $\beta_P$, $\beta_D$ and $n_v$, Eq. (35) falls into a system of linear equations:

$$\Psi X = \Gamma + \Delta \tag{36}$$

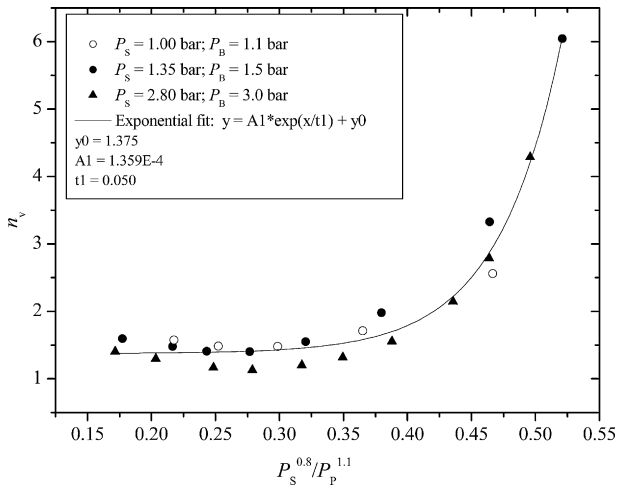


**Fig. 5.** Relation between $n_v$ and ejector working pressures.

where $X$ is the parameters matrix to be determined, $\Delta$ is the measurement or simulation error. Matrixes of $X$, $\Psi$, $\Gamma$ are written as

$$X = \begin{bmatrix} A_1 \\ A_2 \\ A_3 \end{bmatrix}; \qquad \Gamma = \begin{bmatrix} n_v^2 \\ n_v^2 \\ \vdots \\ n_v^N \end{bmatrix}; \qquad \Psi = \begin{bmatrix} \exp(\beta_P^1/0.05) & \beta_D^1 & 1 \\ \exp(\beta_P^2/0.05) & \beta_D^2 & 1 \\ \vdots & \vdots & \vdots \\ \exp(\beta_P^N/0.05) & \beta_D^N & 1 \end{bmatrix} \tag{37}$$

The best estimate $X^*$ of $X$ can be found using the standard least squares method proposed by Young [28] as

$$X^* = (\Psi^T\Psi)^{-1}\Psi^T\Gamma \tag{38}$$

In this work, based on the four ejector geometries and 32 working conditions, the parameters $A_1$, $A_2$ and $A_3$ are obtained using the above parameter identification method. Substituting the parameters into Eq. (35), the velocity exponent $n_v$ is finally achieved as

$$n_v = 1.393 \times 10^{-4} \exp(\beta_P/0.05) + 0.456\beta_D + 0.1668 \tag{39}$$

The correlation of $n_v$ in Eq. (39) is obtained based on various PEM ejector operating conditions and geometries in the ranges of $1.75 \le P_P \le 10.5$ bar, $1.0 \le P_S \le 2.8$ bar, $1.1 \le P_B \le 3.0$ bar, $2.1 \le D_t \le 3.2$ mm and $5.2 \le D_m \le 8.0$ mm. Furthermore, the correlation of $n_v$ only consists of four measurable variables: $P_S$, $P_P$, $D_m$ and

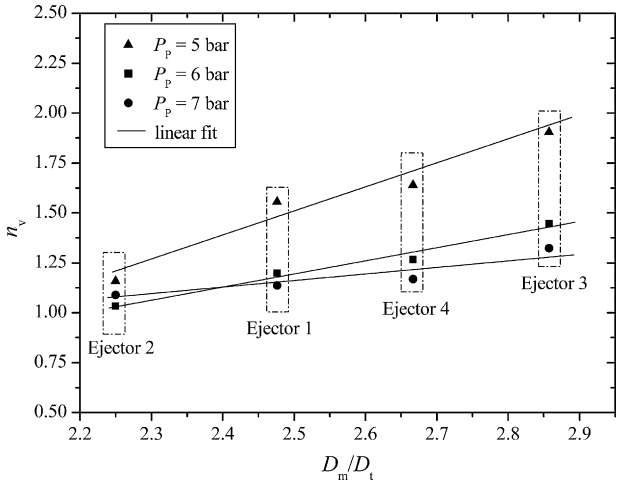


**Fig. 6.** Relation between $n_v$ and ejector geometries.

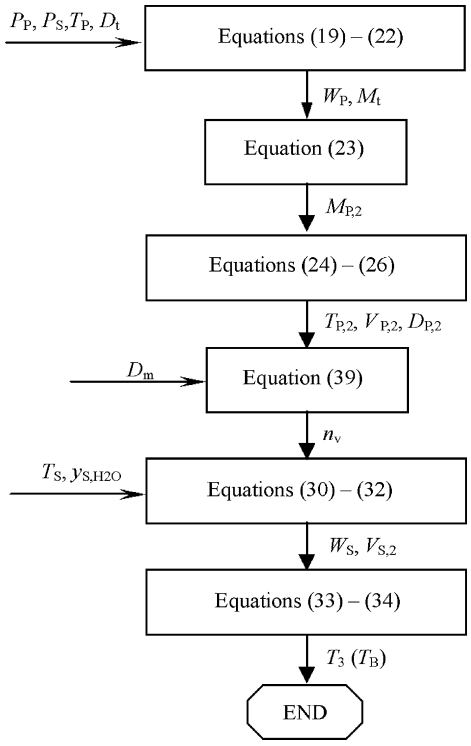


**Fig. 7.** Solution procedure of the ejector model.

$D_t$. Therefore, the Eq. (30) for calculating $W_S$ will be convenience to use in practice.

## 5. Model application

For a given ejector geometry, its performance depends on the pressure $P_P$ and $P_S$, temperature $T_P$ and $T_S$, chemical composition of inlet fuel and anodic recycle gas. The outputs of the ejector model used in PEM fuel cell systems will be the primary mass flow rate $W_P$, the secondary mass flow rate $W_S$, recirculation ratio, temperature and chemical compositions at ejector exit. The solution procedure of the ejector model is given in Fig. 7.

Starting with the same input conditions $P_P$, $P_S$, $T_P$, $T_S$ and $y_{S,H_2O}$, results such as $W_P$, $W_S$ and $T_B$ are obtained from the ejector model and CFD simulation. Comparisons of $W_P$, $W_S$ and $T_B$ between the model and CFD simulation are presented Fig. 8(a)–(c), respectively. It is found that the predicted $W_P$ and $T_B$ by present model match fairly well those from the CFD simulation data. The average derivations of $W_P$ and $T_B$ between model and CFD simulation are 0.63% and 0.28%, respectively. Note that the flow characteristic of the secondary flow is complicated so that $W_S$ is difficult to predict particularly when the ejector works at the subcritical mode. In Fig. 8(c), it can be seen that the new ejector model provides reliable results in predicting $W_S$. The average derivation between model and CFD simulation is 7.25% for all the tested working conditions.

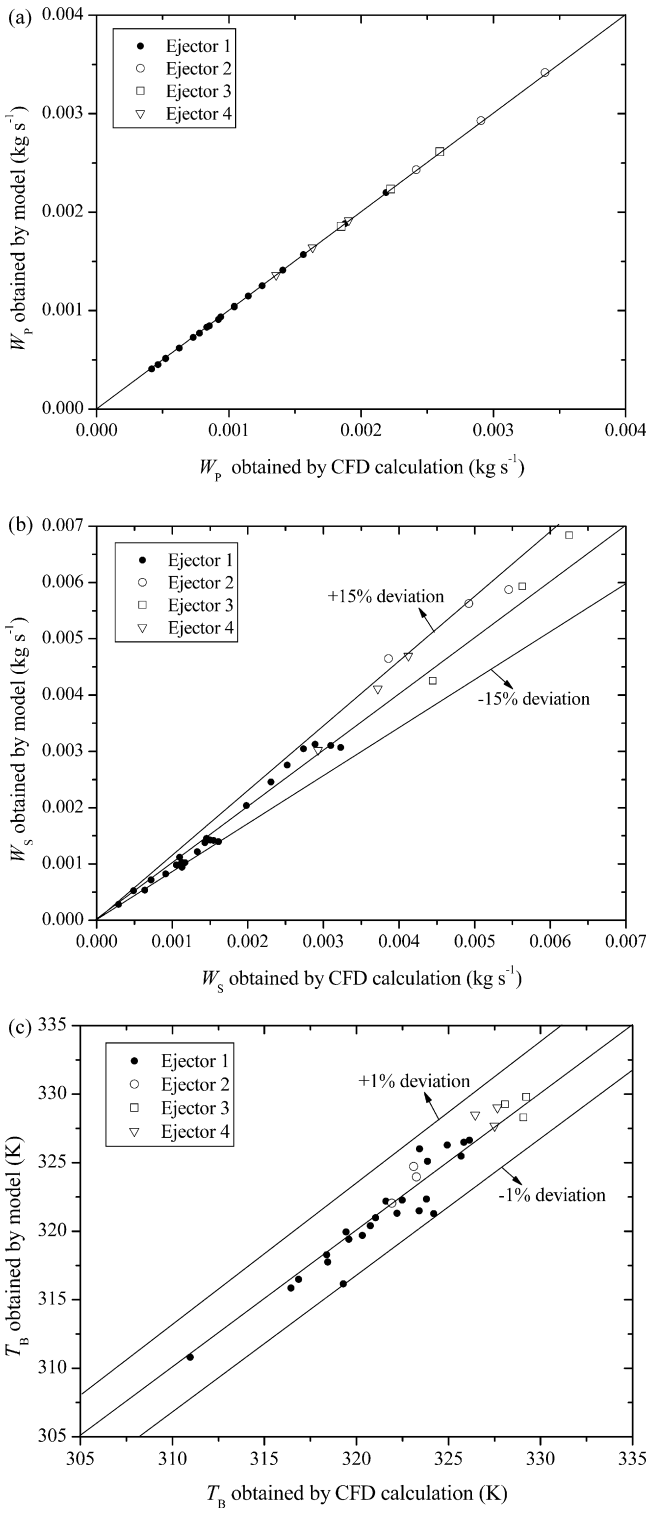


**Fig. 8.** Comparison of results between CFD simulation and model. (a) Mass flow rate of the primary flow; (b) mass flow rate of the secondary flow; (c) ejector exit temperature.

## 6. Results and discussions

As an example, Table 2 shows typical values for a PEM fuel cell system. The ejector 1 in Table 1 is adopted in the following analysis. Starting with these data, the steady-state performances of the ejector and fuel cell system are studied. In order to simplify the analysis, it is assumed that the stack temperature is constant 353 K. All the gases are considered as the ideal gas, and the temperature variation of gas properties is neglected. For simplicity, the air stoichiometric ratio is chosen to be constant 2, and the relative humidity at the humidifier exit is kept at 80%.

### 6.1. Ejector performance

Performances of the ejector and fuel cell stack can be analyzed by varying the stack current and anode pressure. In this study,

**Table 2**
Model parameters.

| Description | Value |
|---|---|
| Cell active area ($m^2$) | 0.1 |
| Cell number | 381 |
| Membrane thickness (m) | $127 \times 10^{-6}$ |
| Membrane equivalent weight ($kg\,mol^{-1}$) | 1.1 |
| Membrane density ($kg\,m^{-3}$) | 2000 |
| Hydrogen inlet temperature, $T_P$ (K) | 298 |
| Cathode inlet oxygen relative humidity (%) | 100 |
| Anode inlet relative humidity (%) | 80 |
| Stack operating temperature (K) | 353 |
| Humidifier temperature (K) | 353 |
| Anode pressure (bar) | 3.0 |
| Cathode inlet pressure (bar) | 3.0 |
| Anode inlet flow coefficient ($kg\,s^{-1}\,Pa^{-1}$) | $0.3 \times 10^{-6}$ |
| Anode outlet flow coefficient ($kg\,s^{-1}\,Pa^{-1}$) | $0.3 \times 10^{-6}$ |
| Cathode inlet flow coefficient ($kg\,s^{-1}\,Pa^{-1}$) | $2.3 \times 10^{-6}$ |
| Cathode outlet flow coefficient ($kg\,s^{-1}\,Pa^{-1}$) | $2.3 \times 10^{-6}$ |
| Volume of lumped cathode ($m^3$) | $10.8 \times 10^{-3}$ |
| Volume of lumped anode ($m^3$) | $9.6 \times 10^{-3}$ |

eleven different stack currents are selected. Results for analysis of the anode recirculation line are shown in Figs. 9–11.

The behavior of $P_P$, $P_S$ and $P_B$ at different stack currents are shown in Fig. 9. It can be seen that $P_P$ rises as the current increases, evidently because raising $P_P$ will increases the mass flow rate of the fuel hydrogen. The behavior of $P_P$ for a convergent–divergent nozzle ejector at the same conditions is also depicted as the dash line in Fig. 9. Compared of $P_P$ between the convergent ejector and convergent–divergent nozzle ejector, it is found that there exists a divergent position at about $P_S/P_P = 0.528$. This is in line with the thermodynamic principles that the critical pressure ratio $\upsilon_{cr}$ is 0.528 for a convergent nozzle with a diatomic molecule as the working fluid. In Fig. 9, the pressure lift in the ejector increases with the stack current, because the pressure loss in the PEM fuel cell has direct ratio with the mass flow rate (i.e. the stack current).

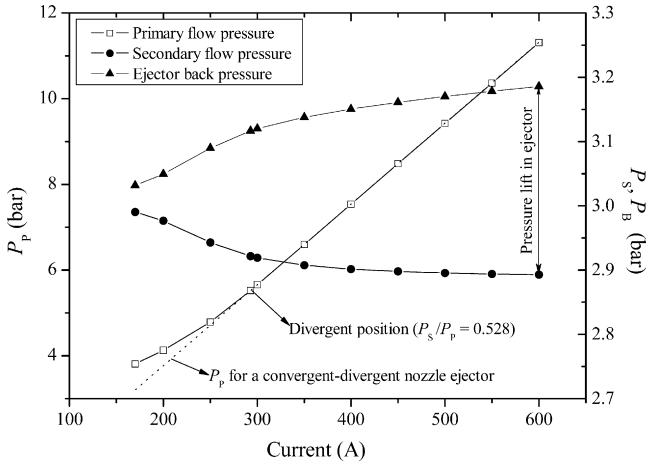


**Fig. 9.** Pressures at anode recirculation line with different stack currents.

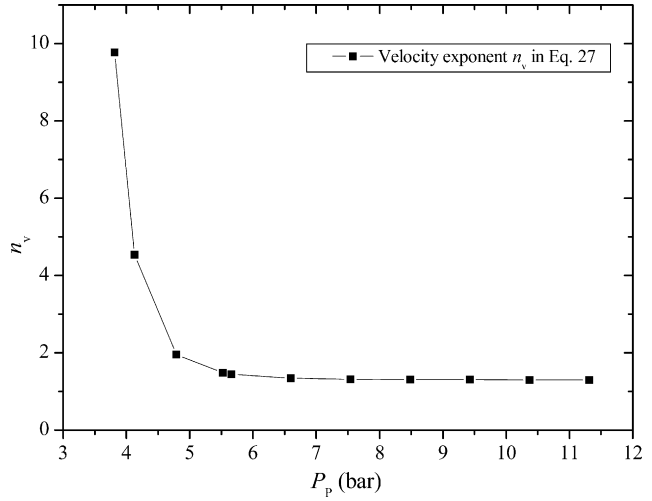


**Fig. 10.** Velocity exponent $n_v$ at different primary flow pressures.

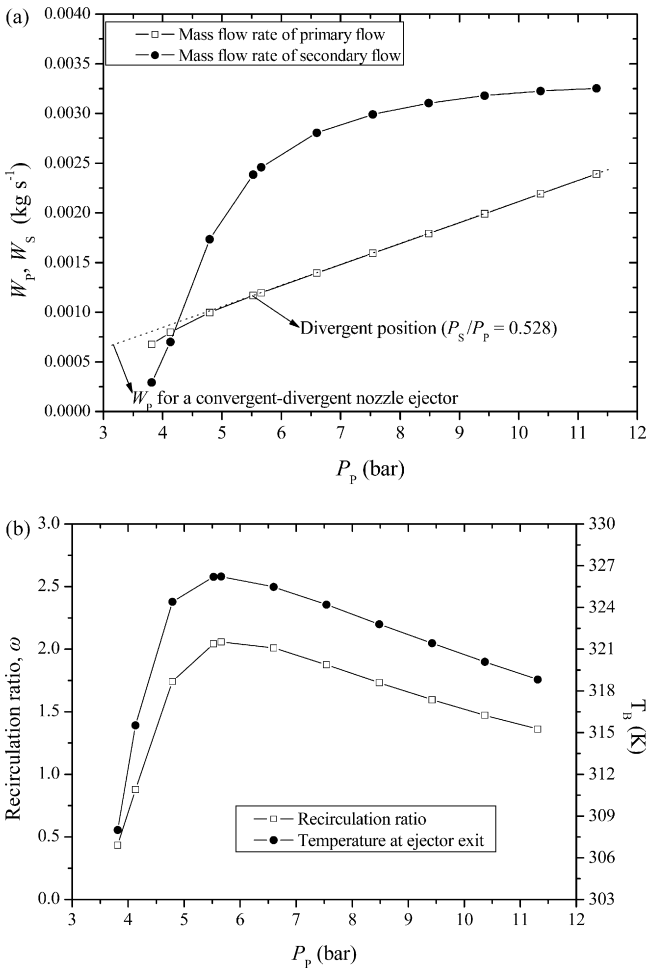


**Fig. 11.** Ejector performances at different primary flow pressures. (a) Mass flow rates; (b) Ejector recirculation ratio and exit temperature.

The velocity exponent $n_v$ is shown in Fig. 10. It is found that that $n_v$ is very sensitive to the primary flow pressure in the low pressure regions, and becomes near constant at high pressure regions. This is because that the ejector works in the subcritical mode when the primary flow pressure is low as shown in Fig. 2(b).

The ejector performances at different stack currents are shown Fig. 11. The characteristics of $W_P$ and $W_S$ in Fig. 11(a) are very similar to the previous experimental and numerical data in Refs. [6,8]. $W_P$ in the convergent ejector is different from that of the convergent–divergent nozzle ejector when $P_S/P_P$ is greater than 0.528. $W_S$ remains quite constant in the high primary flow pressure region.

The ejector recirculation ratio $\omega$ and ejector exit temperature are shown in Fig. 11(b). The ejector has a good recirculation capability ($\omega > 2$) when the primary flow pressure is greater than 5 bar. It is important to note that the recirculation performance will decline once the ejector works at subcritical mode.

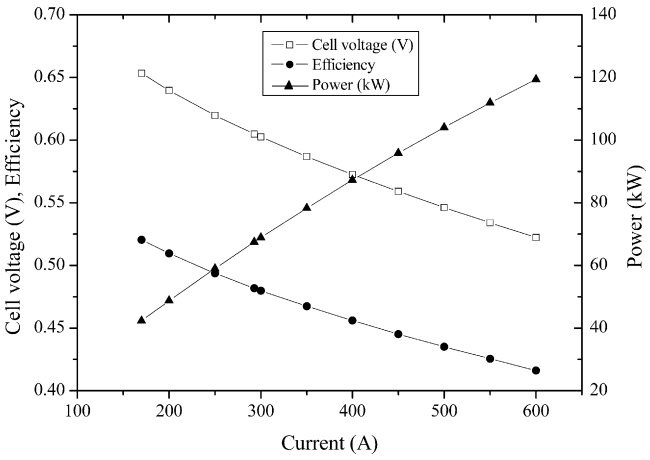


**Fig. 12.** Fuel cell performances at different stack currents.

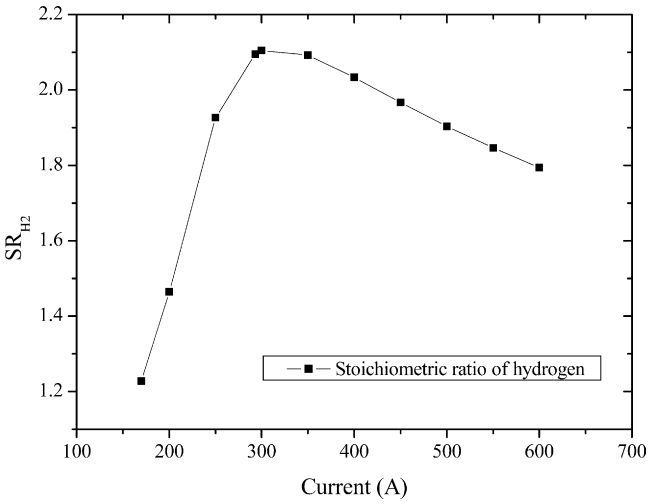


**Fig. 13.** The hydrogen stoichiometric ratio at different stack currents.

### 6.2. Fuel cell performance

Performances of the PEM fuel cell system are analyzed by varying the stack currents as shown in Figs. 12–14. In Fig. 12, the performance properties of the fuel cell stack: voltage, power and stack efficiency are illustrated at different currents. The stack efficiency increases with an increase of the current, and the cell voltage and power decrease as the current increases. Although the ejector performances are affected by the stack current as in Fig. 11, the behaviors of these performance properties agree with the performance characteristics of a typical PEM fuel cell stack. This is because that the hydrogen stoichiometric ratio changes correspondingly as shown in Fig. 13. From Figs. 11 and 13, it can be seen that the hydrogen stoichiometric ratio has a similar trend with the ejector recirculation ratio. The greater recirculation ratio, which means the more unconsumed hydrogen recycled into the anode, leads to the larger hydrogen stoichiometric ratio. In order to adjust the hydrogen stoichiometric ratio, a bypass blower may be required.

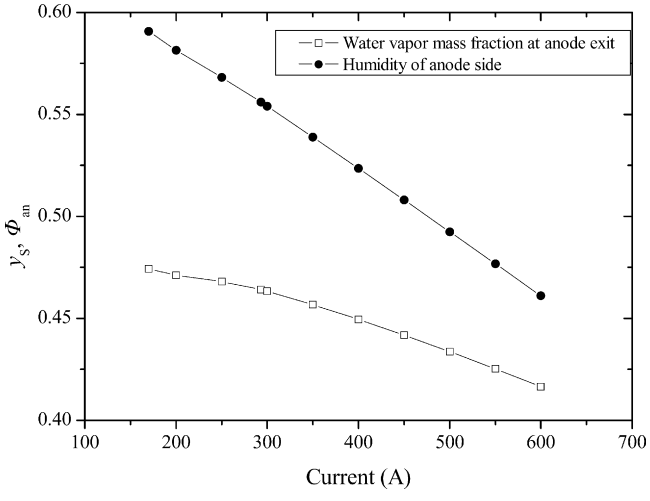


**Fig. 14.** Humidity and vapor mass fraction of anode at different stack currents.

The relative humidity and the water vapor mass fraction at the anode are shown in Fig. 14. No water vapor is condensed in the anode flow channel due to the high current. The relative humidity decreases with an increase of the stack current, resulting in a decrease of the water vapor mass fraction. Both of them will affect the ejector performance, which implies that fluctuations in the anode channel will feedback to the fuel cell stack via the ejector.

## 7. Conclusions

A new theoretical model for the convergent nozzle ejector used in the anode recirculation line of PEM fuel cell systems was proposed in this paper. A concave 2D velocity function is constructed by considering the working conditions and flow characteristic of the PEM ejector. A method for determining the exponent of the velocity function $n_v$ was presented by using the numerical CFD technique with data regression and parameter identification treatments.

Based on the 2D velocity function, the proposed modeling technique can provide more accurate evaluations of the ejector performances than the conventional 1D "constant pressure mixing" and "constant area mixing" ejector modeling theories. The new model was capable of analyzing the ejector performances such as the primary mass flow rate, the secondary mass flow rate, the recirculation ratio and the ejector exit states in not only the critical mode but also subcritical operational mode.

## References

[1] D. Cheddie, N. Munroe, J. Power Sources 147 (2005) 72–84.
[2] M. Uzunoglu, M.S. Alam, Energ. Conserv. Manage. 48 (2007) 1544–1553.
[3] P. Rodatz, A. Tsukada, M. Mladek, L. Guzzella, Proceeding of the 15th IFAC Triennial World Congress, Barcelona, Spain, July, 2002.
[4] B.J. Huang, J.M. Chang, C.P. Wang, V.A. Petrenko, Int. J. Refrig. 22 (1999) 354–364.
[5] B.J. Huang, J.M. Chang, Int. J. Refrig. 22 (1999) 379–388.
[6] Y. Bartosiewicz, Z. Aidoun, P. Desevaux, Y. Mercadier, Int. J. Heat Fluid Fl. 26 (2005) 56–70.
[7] I.W. Eames, S. Aphornratana, H. Haider, Int. J. Refrig. 18 (1995) 378–386.
[8] D.-W. Sun, Energ. Source 19 (1997) 349–367.
[9] Y.H. Zhu, W.J. Cai, C.Y. Wen, Y.Z. Li, Energ. Convers. Manage. 48 (2007) 2533–2541.
[10] F. Marsano, L. Magistri, A.F. Massardo, J. Power Sources 129 (2004) 216–228.
[11] M.L. Ferrari, A. Traverso, L. Magistri, A.F. Massardo, J. Power Sources 149 (2005) 22–32.
[12] Y.H. Zhu, W.J. Cai, C.Y. Wen, Y.Z. Li, J. Power Sources 173 (2007) 437–449.
[13] Y.H. Zhu, W.J. Cai, Y.Z. Li, C.Y. Wen, J. Power Sources 185 (2008) 1122–1130.
[14] A.Y. Karnik, J.S. S Sun, Proceedings of Fuel Cell 2005 Third International Conference on Fuel Cell Science Engineering and Technology, Ypsilanti, MI, May, 2005.
[15] A.Y. Karnik, J. Sun, J.H. Buckland, Proceedings of the American Control Conference, Minneapolis, Minnesota, June, 2006.
[16] C. Bao, M. Ouyang, B. Yi, Int. J. Hydrogen Energ. 31 (2006) 1879–1896.
[17] J. He, S.-Y. Choe, C.-O. Hong, J. Power Sources 185 (2008) 973–984.
[18] T.E. Springer, T.A. Zawodzinski, S. Gottesfeld, J. Electrochem. Soc. 138 (1991) 2334–2342.
[19] A.Y. Karnik, A.G. Stefanopoulou, J. Sun, J. Power Sources 164 (2006) 590–605.
[20] S. Dutta, S. Shimpalee, J.W. Van Zee, Int. J. Heat Mass Transf. 44 (2001) 2029–2042.
[21] M.W. Fowler, R.F. Mann, J.C. Amphlett, B.A. Peppley, P.R. Roberge, J. Power Sources 106 (2002) 274–283.

[22] T. Berning, N. Djilali, J. Power Sources 124 (2003) 440–452.
[23] R. Chahine, F. Laurencelle, J. Hamelin, K. Agbossou, M. Fournier, T.K. Bose, A. Laperriere, Fuel Cells 1 (2001) 66–71.
[24] J. Hamelin, K. Agbossou, A. Laperriere, T.K. Bose, Int. J. Hydrogen Energ. 26 (2001) 625–629.
[25] R. Cownden, M. Nahon, M.A. Rosen, Int. J. Hydrogen Energ. 26 (2001) 615–623.
[26] Y.H. Zhu, W.J. Cai, C.Y. Wen, Y.Z. Li, Appl. Therm. Eng 29 (2009) 898–905.
[27] E. Rusly, L. Aye, W.W.S. Charters, A. Ooi, Int. J. Refrig. 28 (2005) 1092–1101.
[28] P.C. Young, Automatica 6 (1970) 271–287.